Visualizing lithium dendrite formation within solid-state electrolytes

Minghao Sun,[†] Tiefeng Liu,[¶] Yifei Yuan,[‡] Min Ling,[†] Nan Xu,[†] Yanyan Liu,[†] Lijing Yan[†], Hui Li[†], Chengyong Liu,[§] Yingying Lu[†], Yao Shi[†], Yi He[†], Yongsheng Guo[§], Xinyong Tao,[¶] Chengdu Liang[†§*], Jun Lu[‡*]*

[†]*Zhejiang Provincial Key Laboratory of Advanced Chemical Engineering Manufacture Technology, College of Chemical and Biological Engineering, Zhejiang University, Hangzhou 310027, P. R. China;*
[¶]*College of Materials Science and Engineering, Zhejiang University of Technology, Hangzhou 310014, China*
[‡]*Chemical Sciences and Engineering Division, Argonne National Laboratory, 9700 Cass Ave, Lemont, IL 60439, USA;*
[§]*Research Institute, Contemporary Amperex Technology, Limited, Ningde 352000, P. R. China;*

ABSTRACT

Solid-state electrolyte (SSE) is promising for application in all-solid-state lithium metal batteries due to its reliable safety and longevity. The failure of solid-state electrolyte (SSE) to suppress dendrite formation of Li metal anodes has been conventionally explained by uneven Li deposition at Li/SSE interfaces and its subsequent dendritic growth. While Li deposition within SSE has been recently proposed as another key cause for SSE failure, little is known regarding the Li growth details inside SSE itself. In this work, we performed *in-situ* microscopic observation of Li deposition inside SSE and obtained visualized evidences regarding the dynamic process of Li dendrite formation and growth. Li is seen to directly nucleate and propagate within the SSE, leading to its structural cracking. Such behavior should be caused by the presence of P- and S-based crystalline defects in Li_3PS_4 SSE, which is consistent with the cryo-transmission electron microscopy observations and theoretical calculations. This observation provides important insights into the growth mechanisms of Li dendrites within a working lithium battery.

TOC GRAPHICS

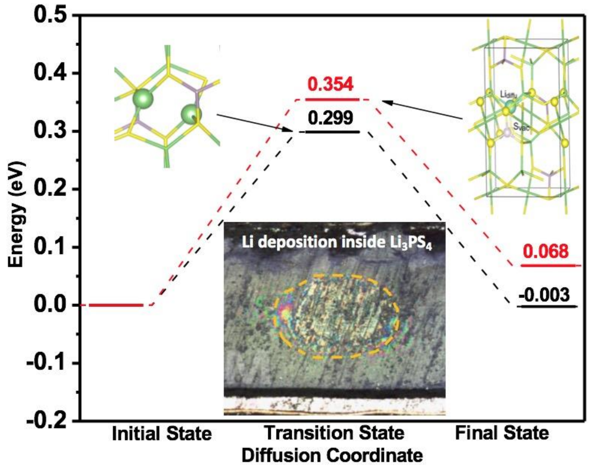

Introduction

Featured by high specific capacity (3860 mAh g^{-1}) and the lowest negative electrochemical potential (-3.04 V vs. SHE), lithium (Li) metal is considered as the ultimate choice of battery anode for high-energy-density energy storage systems[1-4]. Presently, during an electrochemical Li plating process, the dendrite growth is problematic to the Li metal anode[5-8]. Such a behavior incurs a low coulombic efficiency and severe safety risk of assembled Li metal batteries (LMBs)[9-12]. As for its formation, most of understandings and assumptions are originally based on observation in the liquid or polymer electrolytes where the dendrites result from the Li nucleation and uneven deposition on Li/electrolyte interface[13, 14]. As such, for the past many years, the researchers have developed various conceptual strategies, such as enhancing interfacial compatibility and developing solid-state electrolyte (SSE) to deal with the adverse effect of Li dendrites[7, 15, 16].

Among, the SSE has gained significant research interest because of its high mechanical rigidity to hinder Li dendrite growth[17, 18]. Yet, recent study has reported the penetration of metallic Li into SSE materials[19], which has been explained by uneven Li deposition at Li/SSE interfaces and rapid dendrite growth through the SSE[20-23]. During the charging processes, owing to the inhomogeneous contact between SSE and Li metal, interfacial voids (*i.e.*, pores and cracks) tend to be first filled by Li protuberances as the Li nuclei [7, 20, 24, 25]. As the local current density is maximized and the electric field is concentrated at the Li protuberances, Li will preferentially deposit at these sites during subsequent charging[26]. However, it is surprising to observe that Li dendrites still grow at the Li/SSE interfaces that are finely polished, at the modified grain boundaries and even at the surfaced of single-crystalline SSE[27], which cannot be simply explained by the above "inhomogeneous Li/SE interface" theory.

Until very recently, there are some noteworthy exceptions in literature, contradicting the conventional understanding of dendrites stemming from the Li/SSE interface[28]. Han and coworkers found that the direct reduction of Li ions could occur within the SSE during charging/discharging process as a result of nonnegligible electronic conductivity of SSE[29]. Wang *et al.* also demonstrated that high electronic conductivity of the SSE leads to the metallic Li dendrite growth in the bulk (grain and grain boundary)[30]. Decreasing the electronic conductivity is thus considered to be an effective approach to limit the metallic Li dendrite. In spite of the recent studies focusing on Li dendrite growth within SSE, the fundamental understanding of such growth behavior is quite limited due to lack of direct observation in contrast to the few indirect *in situ* characterizations[31, 32]. Therefore, compared with well-established Li dendrite formation mechanism in Li/electrolyte interface, the recognition of the Li deposition process in SSE is still in its infancy, calling for more explorations in the formation mechanism of Li dendrites in SSE[5].

Here, we carried out direct *in-situ* cross-sectional microscopic observation of the Li growth behaviors within the SSE and further corroborated such observations by cryo-transmission electron microscope microscopy (cryo-TEM) and theoretical simulations. We observed that Li nucleation and growth could directly occur inside the SSE. These visualized evidences regarding Li deposition and dendrite propagation in the SSE unraveled their adverse impacts on the structural integrity of SSE. We thus proposed that the nucleation and local growth of Li dendrites inside the SSE lead to its cracking and failure. Furthermore, this mechanism occurs prior to the Li dendrite formation at the Li/SSE interface. This work is thus expected to call for more research attention and effort to address the Li dendrite growth problem.

The Li_3PS_4 (LPS) was considered as the key component in solid-state battery due to its high Li^+ conductivity (*ca.* 10^{-4} S cm^{-1}) and low electron conductivity (2.2×10^{-9} S cm^{-1}). The X-ray diffraction (XRD) measurements shows that the as-prepared LPS SSE belongs to the β-phase

(PDF#76-0973) crystalline structure (Figure S1a), which is consistent with the previous report. Particle size of the LPS is in the range from 5 to 10 μm as shown in Figure S1b. Analysis of energy-dispersive X-ray (EDX) spectroscopy also revealed the uniform distribution of elemental P and S in the LPS SSE (Figure S2). High-resolution transmission electron microscopy (HRTEM) and selected-area electron diffraction (SAED) patterns revealed the polycrystalline structure of the LPS particles (Figure S3). The LPS material has a specific surface area of 15.32 m^2 g^{-1} and an average pore diameter of 34.24 nm (Figure S4).

The laminate of LPS SSE was firstly fabricated by high pressure of 300 MPa. NCM, LPS laminate and Li metal foil (thickness of 50 μm) with round discs (diameter of 8 mm) were assembled into Li/LPS/NCM cell. In detail, a cathode disc was attached to one side of the LPS and cold pressed at 450 MPa for 2 min. And then, Li metal disc was attached onto the other side of the electrolyte disc and cold pressed at 50 MPa for 10 s to assemble the Li/LPS/NCM cell. Traditionally, Li deposition inside SSE is determined either via ex situ observations (e.g., second electron mode or backscattered electron mode of a scanning electron microscope) or inferred from in situ characterization results (e.g., neutron depth profiling)[20, 26, 33, 34]. However, due to the instability of Li metal and SSE toward moisture and O_2, the specimens will corrode and deform during the transfer process at the ambient environment, limiting achieving a correct understanding of the Li deposition process inside SSE.

To enable direct observation of the evolving process of Li deposition inside SSE, we carried out a cross-sectional *in situ* optical microscopic observation technique for a Li/LPS/NCM cell, as shown in Figure S5. The assembled Li/LPS/NCM cell was charged at a constant current density of 100 μA cm^{-2}. A typical charging platform profile from 3.6 to 4.2 V was collected (Figure 1a), in which no sharp polarization of voltages or shorting could be detected, allowing us to visualize the Li distribution inside SSE during the entire charging process. In Figure 1b-g, the deposition process of Li inside LPS is depicted by a series of cross-sectional snapshots taken at 0, 3, 6, 9, 12 and 18 h of the charging process. As shown in Figure 1b, no Li dendrites are formed at the Li/SE interface before charging, while the SSE are detached from the Li metal anode quickly as the charging process begins, a process that might be attributed to the volumetric expansion of SSE in the regions outside of the camera field, excluding the possibility of Li deposition induced by the Li/SE interface within the camera vision.

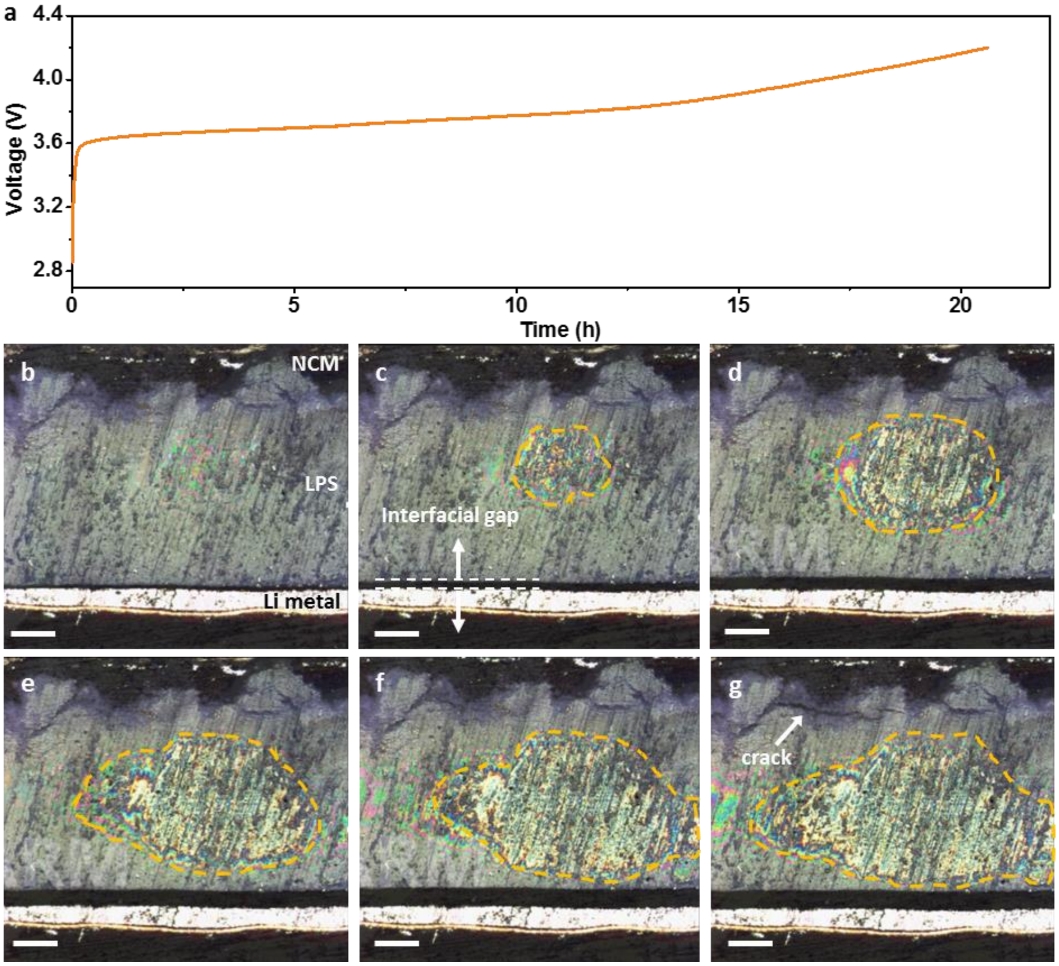

Figure 1. *In situ* optical observation of the “point-to-surface” Li deposition process inside LPS. (a) A typical charging profile of a Li/LPS/NCM cell without obvious cracks generated in LPS. (b-g) Cross-sectional snapshots of the cell in (a) taken at 0 (b), 3 (c), 6 (d), 9 (e), 12 (f) and 18 h (g) of the charging process. Scale bars: 100 μm.

After 3 h, local Li reduction appeared in LPS SSE (Figure 1b). The LPS SSE detached increasingly from Li metal anode is an indication that the insert of Li dendrites incurs the volume exploration of LPS SSE. Consequently, local Li concentration rapidly increased as the decreasing cross-sectional areas between Li anode and LPS SSE. As the charging process continues, the area of Li reduction gradually increased and the interfacial gap between Li anode and LPS SSE also slowly enlarged (Figure 1c, d). The growth of metallic Li in bulk of LPS can enhance the electron conductivity of the corresponding region. Therefore, the subsequent reduction of Li ions from LPS SSE preferentially appears around the deposited Li metal, forming silver-like Li area (Figures 1e-g and Video S1). No evident dendrite formation was observed on anode surface. In addition, the occurrence of cracks near the cathode region (indicated by the arrow in Figure 1g) is tentatively caused by the volumetric variation of LPS SSE rather than that of cathodes, considering that the volumetric variation of NCM (2%-4%) is far below the critical value (7.5%). Notably, this structural change of LPS SSE has no obvious influence on electrochemical behaviors of the full cell. Crystalline structure of the LPS SSE is nearly unchanged, as shown in the XRD pattern (Figure S1a).

In parallel, we demonstrate that Li deposition could induce cracking of LPS from the inside, not from the outside, where Li^+ is transferred into a Li/LPS/NCM cell. There are no obvious cracks or Li deposition was observed inside LPS SSE or at the Li/LPS interface at the beginning (Figure 2b). As the charging began, cracks were formed quickly inside SSE and the Li/SE interfaces started to detach (Figure 2c), suggesting Li deposition inside SSE. Next, as more Li is deposited inside SSE, leading to the emergence of new cracks (indicated by the white arrow in Figure 2d, the old cracks and Li/SE interfacial gaps are broadened. There is a small contact area remained to offer the Li^+/electron transfer between LPS SSE and Li metal (inset of Figure 2d). Local Li^+/electron concentration, which obviously induced the formation of Li wire in the contact area, could be regarded as the visual evidence for the Li dendrite formation and growth at the interface (Figures 2e-f). Continuous growth of the Li wire is maintained during the subsequent charging process, elongating with the broadening of the Li/LPS interfacial gap (Figure 2f). Subsequently, when this full cell was performed with a discharging procedure. Obviously, the Li wire is the byproduct of Li/SE interfacial detachment rather than the converse, for the shear modulus of Li metal (2.83 GPa) is much smaller than that of LPS (18-25 GPa)[35]. Moreover, because the Li content is extracted from LPS SSE during the subsequent discharging process, the volumetric shrinkage of LPS SSE induces narrowing of the as-formed cracks (including the Li/SE interfacial gap) and bending of the Li wire (see Video S2), confirming that the cracks in LPS are induced by Li deposition[36]. After a series of charge/discharge procedures, the full cell based on LPS SSE seriously suffer a low coulombic efficiency (Figure S6), indicating a battery failure induced by Li formation dendrite inside LPS SSE.

To achieve deeper insights into Li dendrite formation depending on the rates, in-situ observations of the battery was further performed at the increased current densities of 200, 500 and 1000 μA cm^{-2}. As shown in Video S3, the LPS SSE expands longitudinally in the charging processes, and shrinks accordingly at discharging, which suggests formation and dissolution of Li dendrites in the LPS SSE, respectively. More importantly, a clear correlation could be drawn between the LPS SSE expansion/shrinkage rate and the charging/discharging rate of the battery, namely, the LPS SSE expands/shrinks more violently as the charging/discharging current increases. As such, it's reasonable to conclude that the larger the charging/discharging rate, the faster Li dendrites deposit/dissolute in the LPS SSE. It should be noted that only some small areas of Li dendrite formation could be observed at the cross-sectional surface of the battery, which seems insufficient to induce such violent volumetric variations of the LPS SSE shown in Video S3 and suggests Li dendrite formation beneath the cross-sectional surface. This is also consistent with our hypothesis that Li dendrite formation could be induced by the randomly dispersed atomic scale defects in LPS (see below).

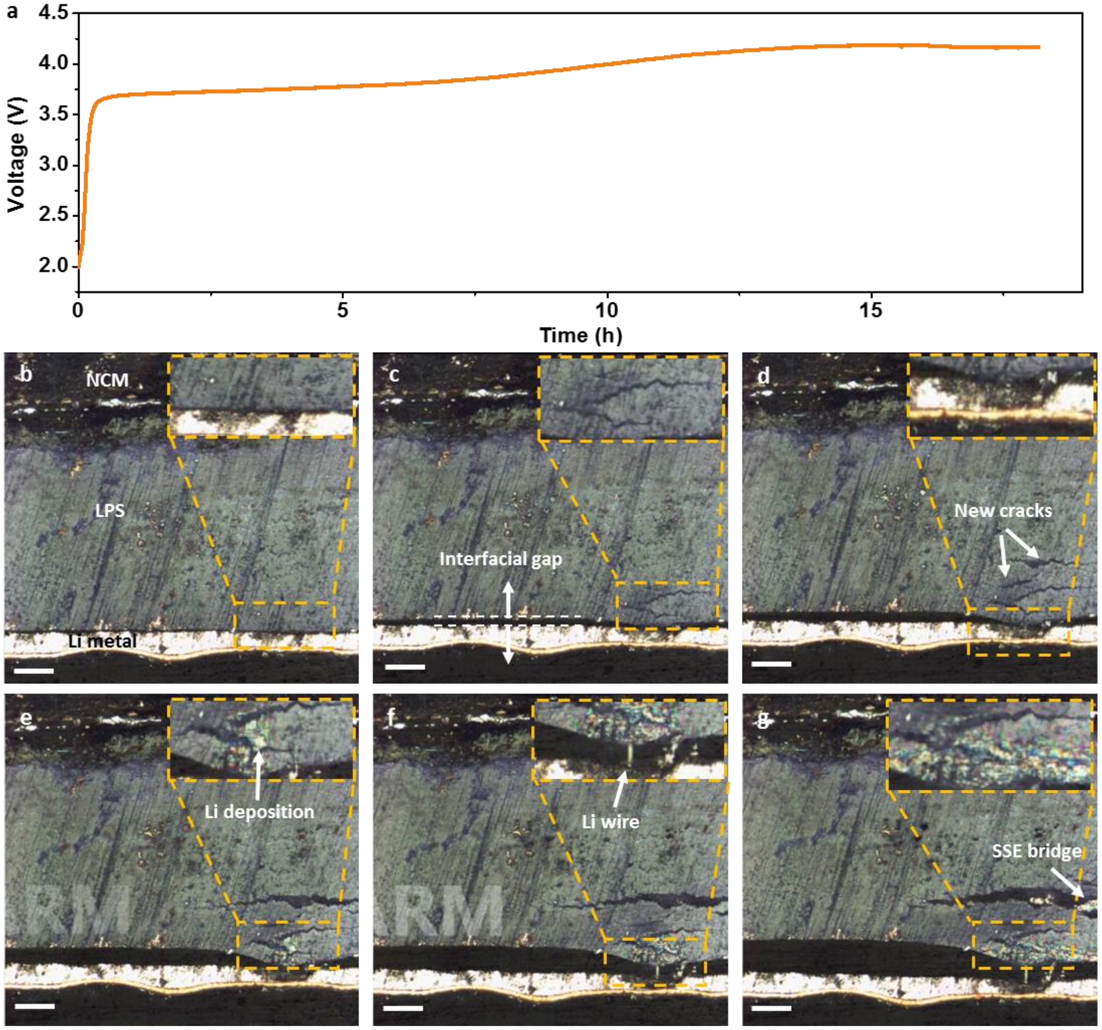

Figure 2. *In situ* optical observation of the crack formation process induced by Li deposition inside LPS. (a) A typical charging profile of a Li/LPS/NCM cell with obvious cracks generated in LPS. (b-g) Cross-sectional snapshots of the cell in (a) taken at the 0 (b), 1 (c), 2 (d), 5 (e), 8 (f) and 18 h (g) of the charging process. Scale bars: 100 μm.

As reported in previous studies, the cracks induced by Li deposition inside SSE tend to become interconnected as the Li deposition accumulates in the bulk of SSE[26]. Meanwhile, the excess chemical potential of Li at the cracks relative to pure Li metal further motivates continuous Li propagation along the cracks, leading to shorting of the cells when the Li deposition in the cracks are interconnected. However, based on the above observations, we speculate on a possible process of LPS SSE for battery failure. During the charging process, the Li uptake within LPS SSE induces the volume expansion and then structural cracks, which commonly tend to become interconnected as the charging proceeds and are favor for continuous propagation of Li deposition in the cracks. Meanwhile, the LPS SSE cracking (including the detaching of Li/SE interface) leads to rapid arrival of cut-off voltage during the charging process of the cells. As the charging proceeds, if the Li deposition in the cracks interconnects before the cell reaches the upper-limit voltage, shortage of the cell is eminent. However, if the cell reaches the upper-limit voltage ahead of the Li deposition interconnecting in the bulk of SSE, shortage of the cell could be prevented.

To further reveal the origins regarding the Li appearance inside LPS SSE, it is prerequisite to confirm Li nucleation within LPS. Normally, metallic Li is difficult to be observed due to its high sensitivity to high intensive electron beam of HRTEM. Recently, the cryo-TEM technique has been proven for its feasibility for observing Li metal[37]. The Cu grid is used as the substrate for the LPS electrolyte. Initially, some LPS SSE was dispersed in Cu grid. The resultant Cu grid was subsequently added into the interlayer by two LPS SSEs. After the charge procedure, such a Cu grid was collected and observed using the Cryo-TEM technique under the temperature of -180 ºC. Based on morphological observations before and after Li deposition in LPS SSE, the LPS SSE expanded evidently (Figure 3a, b). The HRTEM image of the LPS was clearly shown in Figure 3c. The interplanar spacing of 3.0 Å matched well with the (221) plane of LPS. Similarly, the crystalline Li, Li_2CO_3 and P can be detected as evidenced by their (110), (002) and (111) crystal planes, respectively. Besides, the fast fourier transform (FFT) in Figure 3d reconfirmed the existence of the LPS crystal, Li metal and inorganic Li compounds. This phenomenon indicates that Li nucleates in the LPS SSE, and may grow with the increase of circulation.

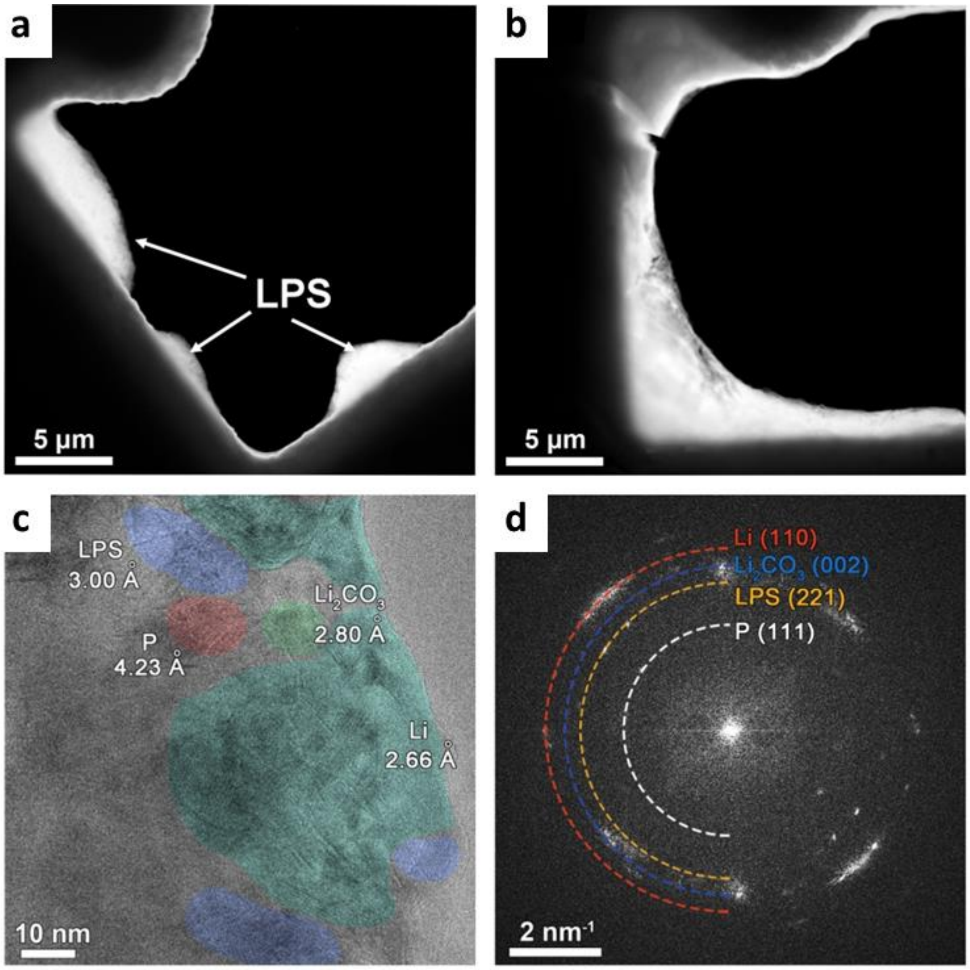

Figure 3. Cryo-TEM for the LPS observation**.** (a, b) STEM images illustrating morphological change before and after Li deposition in LPS SSE. (c) HRTEM image of LPS SSE after charge. (d) The corresponding FFT of (c).

Normally, Li reduction within the SSE requires simultaneously high electron/ion concentration for the initial Li nucleation. While the electronic conduction of SSE has been generally considered to be low, we propose here that the crystalline defects such as S and P vacancies in LPS SSE should be responsible for the nonnegligible electron conduction. To testify this hypothesis, Density functional theory (DTF) is used to evaluate the ability of electronic transfer in the LPS phase. The migration pathway or active energy of interstitial Li^+ ions in the SSE with S vacancy and P vacancy were studied respectively. As for Li migration mechanism in perfect β-Li_3PS_4, Generally, two mechanisms are involved in interstitial Li^+ ion migration in the SSE, namely, the direct-hopping mechanism, which refers to an interstitial Li^+ ion migrating along the lattice interstices of the SSE without substituting the lattice atoms, and the knock-off mechanism, in which an interstitial Li^+ ion migrates by substituting and pushing a lattice Li atom into the adjacent interstitial position[38].

The β-Li_3PS_4 unit cell was optimized using a higher convergence precision and the optimized structure is shown in Figure 4a. The PS_4^{3-} tetrahedrons in β-Li_3PS_4 is highlighted in which the lattice Li atom is coordinated with sulfur atoms. Despite the existence of large holes between the adjacent tetrahedrons, the migration energy for Li to migrate through it is as high as 0.735 eV, which is reasonable because the direct-hopping paths along a, b and c directions (Figure 4a) are all separated by the PS_4^{3-} group. By contrast, the knock-off mechanism is thermodynamically more favorable. In this process, the interstitial Li^+ ion migrates by pushing the adjacent lattice Li forward with an energy barrier of only 0.299 eV (Figure 4b). This is consistent with Yang's work, in which the knock-off mechanism is also considered the most favorable mechanism for Li migration in β-Li_3PS_4 SSE[38]. The stable location of the interstitial Li^+ ion is between the sulfur atoms of two tetrahedrons in the c direction, labeled as Li_{diffu} in Figure 4c. Figure 4d illustrates the migration of an interstitial Li^+ ion from the initial position to a centrosymmetric final position by pushing the central adjacent lattice forward. The energy profile along the migration path and configuration of the transition state are shown in the main graph and left inset graph of Figure 4b and 4d, respectively. Next, the interstitial Li^+ ion migrates forward to another stable location of the neighboring image in a reverse way, enabling Li migration in perfect β-Li_3PS_4 by repeating the above knock-off process.

However, the reality is that there are countless defects existing as-synthesized materials including the LPS electrolyte. In the model of Li migration/deposition mechanism in β-Li_3PS_4 with the defects. We studied the migration mechanism of interstitial Li^+ ions in β-Li_3PS_4 with the defects and tried to determine the effects of those defects on triggering Li deposition. Considering that the interstitial Li^+ ions are exotic atoms for the LPS, the sulfur and phosphorus atoms in the nearby PS_4^{3-} tetrahedrons are overcoordinated compared with the regular ones and could also generate atomic-scale vacancies. The migration of interstitial Li^+ ions in the LPS with S vacancy and P vacancy were studied respectively.

For PS_4^{3-} tetrahedrons, the sulfur atoms are negatively charged while the central phosphorus atom is positively charged. Upon encountering an S vacancy during transfer, the interstitial Li^+ ion will be reduced to some extent by gaining electrons from the adjacent S atoms to balance the charge of the local region. Meanwhile, to stabilize the positive charges that the P atoms carry, the P atoms will shift toward the partially reduced interstitial Li^+ ions and shorten the P-Li distance by 0.420 Å compared with those in perfect LPS. The overlapping between the valence state density of P and Li atoms suggests the emergence of new bonds (Figure 4e) that are a hindrance to the migration of interstitial Li. Thus, the migration energy needed to complete the knock-off mechanism increases to 0.354 eV (Figure 4b) and the energy of the final state in the pathway is higher than that of the initial state. Therefore, the migration of interstitial Li^+ ions in LPS with S vacancy is thermodynamically unfavorable, retarding the migration of interstitial Li^+ ions such as traffic jams and initiating Li deposition by providing the trapped Li with electrons.

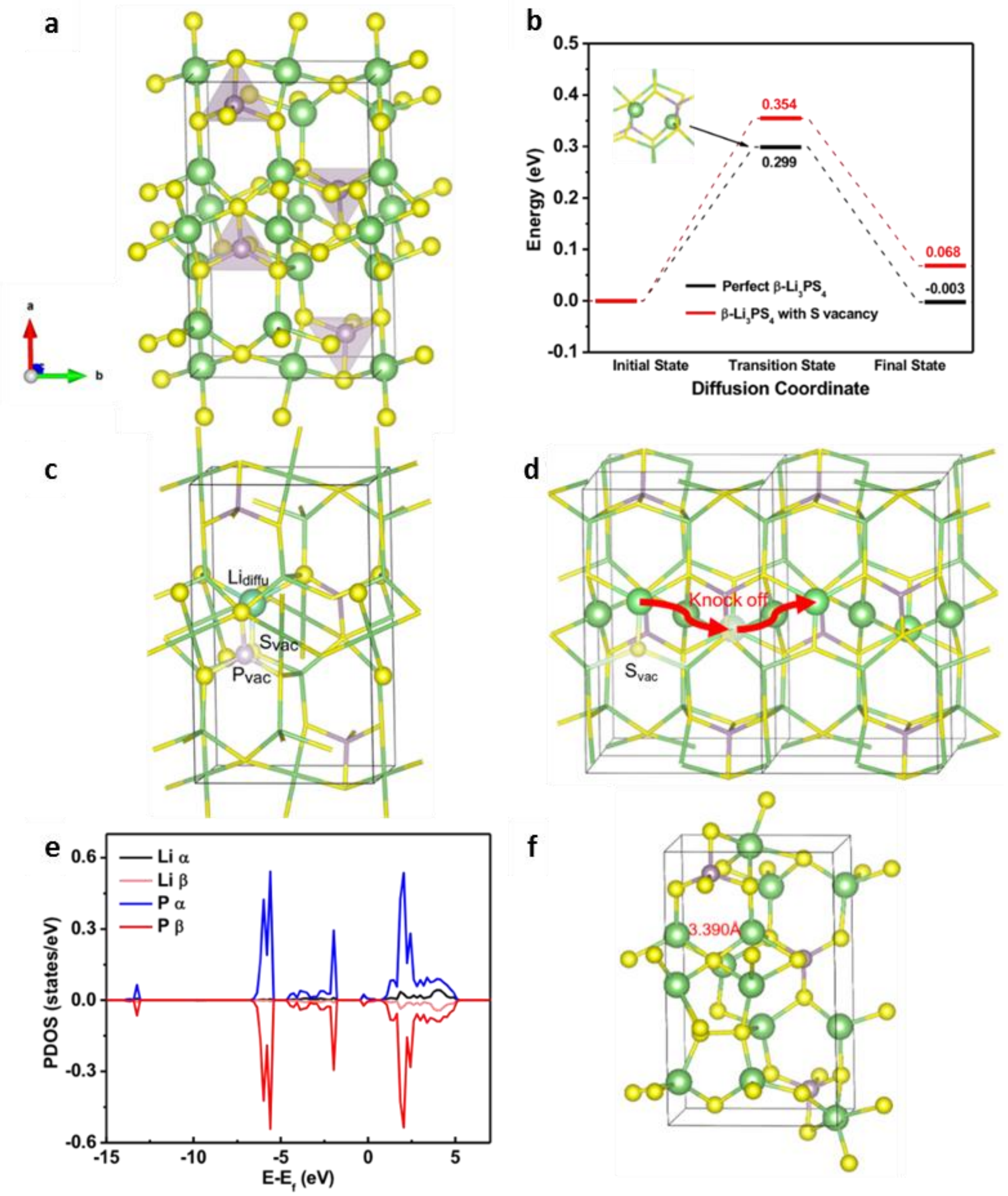

Figure 4. Comparison of the interstitial Li$^+$ ion transfer behaviors in perfect or defective β-Li$_3$PS$_4$. (a) Structure of the optimized β-Li$_3$PS$_4$ unit cell with the PS$_4^{3-}$ subunit highlighted as violet tetrahedrons. (b) Positions of the interstitial ion Li$_{diffu}$, S vacancy S$_{vac}$ and P vacancy P$_{vac}$. Other atoms away from the interstitial ion are hidden for clarity. All structures are visualized using the VESTA package[40]. (c) Comparison of the energy profiles along the migration path in perfect LPS and LPS with S vacancy. The inset graph exhibits the configuration of the migration transition state in perfect LPS. (d) The migration pathway of an interstitial Li$^+$ ion from the initial position to a centrosymmetric final position via a knock-off mechanism in LPS. (e) The density of valence states of the interstitial Li$^+$ ion and central phosphorus atom in LPS with S vacancy. α and β mean spin-up and spin-down orbitals, respectively. (f) The structure of an interstitial Li$^+$ ion inside LPS with P vacancy.

For the P vacancy, lacking a central phosphorus atom renders the PS_4^{3-} tetrahedron electron enrichment region inside the SE lattice. In this case, the interstitial Li^+ ions and lattice Li near the P vacancy would be approached to balance the charge, consequently distorting the lattice structure of LPS. The optimized structure of an interstitial Li^+ ion inside LPS with P vacancy is shown in Figure 4f. The average distance between the interstitial Li^+ ion and lattice Li ions nearby is calculated as 3.390 Å, while the corresponding average distance is 3.787 Å in perfect SSE. A body-centered cubic Li bulk structure from the Materials Project database is used for comparison. Closer to the nearest neighbor distance of 2.966 Å in the bulk, the accumulation of Li is faster and more likely to occur in SSE with P vacancy. Based on the above, we conclude that both S and P vacancies could induce trapping of interstitial Li^+ ions in LPS, while the latter will be reduced by gaining electrons from the SSE during subsequent charging[26], providing nucleation sites for Li deposition. It should be noted that the Li depositions induced by S and P vacancies is consistent with their random distribution in LPS SSE. Meanwhile, the energy barrier of Li nucleation is lower as the temperature decreases, favoring the rapid interconnection of Li depositions and is consistent with the results in previous works[39].

In summary, we for the first time visualized Li nucleation and growth within the SSE and provided reasonable explanation for such interesting behavior. Accompanied with large volume expansion, this behavior adversely impacts the structural integrity of LPS SSE, resulting in the occurrence of cracks. We believe this work can provide the battery community a different view to understand the issues of Li dendrite growth associated with the SSE and more efforts should thus be spent to efficiently address such growth problems within the SSE crystals in addition to the Li/SSE interfaces.

ASSOCIATED CONTENT

Supporting Information.

The Supporting Information is available free of charge on the ACS Publications website at DOI: 10.1021/acsenergylett ((please add manuscript number))

Detailed information on SSE preparation, material and electrochemical measurement, DFT computational method, further electrochemical characteristics and a video file of the in-situ test are also provided.

AUTHOR INFORMATION

Corresponding Authors

*Email: minling@zju.edu.cn (M.L.)

*Email: cdliang@zju.edu.cn (C.D.L.)

*Email: junlu@anl.gov (J.L.)

ORCID

Min Ling: 0000-0001-9132-418X

Jun Lu: 0000-0003-0858-8577

Chengdu Liang: 0000-0002-3017-7785

Yifei Yuan: 0000-0002-2360-8794

Notes

The authors declare no competing financial interest.

ACKNOWLEDGMENT

M.L. acknowledges financial supports from the National Key R&D Program of China (Grant No. 2018YFB0104300). Work at Argonne National Laboratory was supported by the U. S. Department of Energy (DOE), Office of Energy Efficiency and Renewable Energy, Vehicle Technologies Office under Clean Vehicles, US-China Clean Energy Research Centre (CERC-CVC2). Argonne National Laboratory is operated for DOE Office of Science by UChicago Argonne, LLC, under contract number DE-AC02-06CH11357.

REFERENCES

1. Aguesse, F.; Manalastas, W.; Buannic, L.; Lopez Del Amo, J. M.; Singh, G.; Llordes, A.; Kilner, J. *ACS Appl. Mater. Inter.* **2017,** 9, 3808-3816.
2. Liu, T.; Zheng, J.; Hu, H.; Sheng, O.; Ju, Z.; Lu, G.; Liu, Y.; Nai, J.; Wang, Y.; Zhang, W.; Tao, X. *J. Energy Chem.* **2021,** 55, 272-278.
3. Zhang, D.; Dai, A.; Wu, M.; Shen, K.; Xiao, T.; Hou, G.; Lu, J.; Tang, Y. *ACS Energy Lett.* **2020,** 5, 180-186.
4. Shen, K.; Wang, Z.; Bi, X.; Ying, Y.; Zhang, D.; Jin, C.; Hou, G.; Cao, H.; Wu, L.; Zheng, G.; Tang, Y.; Tao, X.; Lu, J. *Adv. Energy. Mater.* **2019,** 9, 1900260.
5. Tikekar, M. D.; Choudhury, S.; Tu, Z.; Archer, L. A. *Nat. Energy* **2016,** 1, 16114
6. Han, F.; Zhu, Y.; He, X.; Mo, Y.; Wang, C. *Adv. Energy Mater.* **2016,** 6, 1501590.
7. Tsai, C. L.; Roddatis, V.; Chandran, C. V.; Ma, Q.; Uhlenbruck, S.; Bram, M.; Heitjans, P.; Guillon, O. *ACS Appl. Mater. Inter.* **2016,** 8, 10617.
8. Ye, H.; Xin, S.; Yin, Y.-X.; Guo, Y.-G. *Adv. Energy Mater.* **2017,** 7, 1700530.
9. Sheng, O.; Zheng, J.; Ju, Z.; Jin, C.; Wang, Y.; Chen, M.; Nai, J.; Liu, T.; Zhang, W.; Liu, Y.; Tao, X. *Adv. Mater.* **2020,** 32, 2000223.

10. Lin, Z.; Liu, T.; Ai, X.; Liang, C. *Nat. Commun.* **2018,** 9, 5262.

11. Li, Y.; Lu, J. *ACS Energy Lett.* **2017,** 2, 1370-1377.

12. Zhang, D.; Dai, A.; Fan, B.; Li, Y.; Shen, K.; Xiao, T.; Hou, G.; Cao, H.; Tao, X.; Tang, Y. *ACS Appl. Mater. Inter.* **2020,** 12, 31542-31551.

13. Cheng, L.; Chen, W.; Kunz, M.; Persson, K.; Tamura, N.; Chen, G.; Doeff, M. *ACS Appl. Mater. Inter.* **2015,** 7, 2073-81.

14. Kim, Y.; Yoo, A.; Schmidt, R.; Sharafi, A.; Lee, H.; Wolfenstine, J.; Sakamoto, J. *Front. Energy Res.* **2016,** 4, 20.

15. Gao, Z.; Sun, H.; Fu, L.; Ye, F.; Zhang, Y.; Luo, W.; Huang, Y. *Adv. Mater.* **2018,** 30, e1705702.

16. Wood, K. N.; Noked, M.; Dasgupta, N. P. *ACS Energy Lett.* **2017,** 2, 664-672.

17. Lou, S.; Zhang, F.; Fu, C.; Chen, M.; Ma, Y.; Yin, G.; Wang, J. *Adv. Mater.*, 2000721.

18. Hatzell, K. B.; Chen, X. C.; Cobb, C. L.; Dasgupta, N. P.; Dixit, M. B.; Marbella, L. E.; McDowell, M. T.; Mukherjee, P. P.; Verma, A.; Viswanathan, V.; Westover, A. S.; Zeier, W. G. *ACS Energy Lett.* **2020,** 5, 922-934.

19. Famprikis, T.; Canepa, P.; Dawson, J. A.; Islam, M. S.; Masquelier, C. *Nat. Mater.* **2019**, 1278–1291.

20. Porz, L.; Swamy, T.; Sheldon, B. W.; Rettenwander, D.; Frömling, T.; Thaman, H. L.; Berendts, S.; Uecker, R.; Carter, W. C.; Chiang, Y.-M. *Adv. Energy Mater.* **2017,** 7, 1701003.

21. Bucci, G.; Swamy, T.; Bishop, S.; Sheldon, B. W.; Chiang, Y.-M.; Carter, W. C. *J. Electrochem. Soc.* **2017,** 164, A645-A654.

22. Yonemoto, F.; Nishimura, A.; Motoyama, M.; Tsuchimine, N.; Kobayashi, S.; Iriyama, Y. *J. Power Sources* **2017,** 343, 207-215.

23. Hong, Z.; Viswanathan, V. *ACS Energy Lett.* **2018,** 3, 1737-1743.

24. Schmidt, R. D.; Sakamoto, J. *J. Power Sources* **2016,** 324, 126-133.

25. Raj, R.; Wolfenstine, J. *J. Power Sources* **2017,** 343, 119-126.

26. Shen, F.; Dixit, M. B.; Xiao, X.; Hatzell, K. B. *ACS Energy Lett.* **2018,** 3, 1056-1061.

27. Porz, L.; Swamy, T.; Sheldon, B. W.; Rettenwander, D.; Frömling, T.; Thaman, H. L.; Berendts, S.; Uecker, R.; Carter, W. C.; Chiang, Y.-M. *Adv. Energy Mater.* **2017,** 7, 1701003.

28. Liu, H.; Cheng, X.-B.; Huang, J.-Q.; Yuan, H.; Lu, Y.; Yan, C.; Zhu, G.-L.; Xu, R.; Zhao, C.-Z.; Hou, L.-P.; He, C.; Kaskel, S.; Zhang, Q. *ACS Energy Lett.* **2020,** 5, 833-843.

29. Han, F.; Yue, J.; Zhu, X.; Wang, C. *Adv. Energy Mater.* **2018,** 8, 1703644.

30. Han, F.; Westover, A. S.; Yue, J.; Fan, X.; Wang, F.; Chi, M.; Leonard, D. N.; Dudney, N. J.; Wang, H.; Wang, C. *Nat. Energy* **2019,** 4, 187-196.

31. Kim, S. H.; Kim, K.; Choi, H.; Im, D.; Heo, S.; Choi, H. S. *J. Mater. Chem. A* **2019,** 7, 13650-13657.

32. Lou, S.; Yu, Z.; Liu, Q.; Wang, H.; Chen, M.; Wang, J. *Chem* **2020,** 6, 2199-2218.

33. Ren, Y. Y.; Shen, Y.; Lin, Y. H.; Nan, C. W. *Electrochem. Commun.* **2015,** 57, 27-30.

34. Bron, P.; Roling, B.; Dehnen, S. *J. Power Sources* **2017,** 352, 127-134.

35. Masias, A.; Felten, N.; Garcia-Mendez, R.; Wolfenstine, J.; Sakamoto, J. *J. Mater. Sci.* **2018,** 54, 2585-2600.

36. Lewis, J. A.; Cortes, F. J. Q.; Boebinger, M. G.; Tippens, J.; Marchese, T. S.; Kondekar, N.; Liu, X.; Chi, M.; McDowell, M. T. *ACS Energy Lett.* **2019,** 4, 591-599.

37. Lee, J. Z.; Wynn, T. A.; Schroeder, M. A.; Alvarado, J.; Wang, X.; Xu, K.; Meng, Y. S. *ACS Energy Lett.* **2019,** 4, 489-493.

38. Yang, Y.; Wu, Q.; Cui, Y.; Chen, Y.; Shi, S.; Wang, R. Z.; Yan, H. *ACS Appl. Mater. Inter.* **2016,** 8, 25229.

39. Akolkar, R. *J. Power Sources* **2014,** 246, 84-89.

40. Momma, K.; Izumi, F. *J. Appl. Crystallogr.* **2011,** 44, 1272-1276.